

Air-Bearing Validation of a Reaction-Wheel Micro-Vibration Framework for High-Performance Imaging Satellites

Marisa du Plessis
*Department of Electrical and
Electronic Engineering
Stellenbosch University*
Stellenbosch, South Africa
marisa@cubespace.co.za

Prof. Willem Herman Steyn
*Department of Electrical and
Electronic Engineering
Stellenbosch University*
Stellenbosch, South Africa
whsteyn@sun.ac.za

Prof. Hendrik Willem Jordaan
*Department of Electrical and
Electronic Engineering
Stellenbosch University*
Stellenbosch, South Africa
wjordaan@sun.ac.za

Abstract—High-performance imaging satellite missions require exceptional pointing stability to ensure image quality and geometric fidelity. This stability is often degraded by micro-vibrations originating from reaction wheels, which propagate through the spacecraft structure and induce line-of-sight (LoS) jitter. This paper presents an air-bearing-based experimental campaign that directly links reaction-wheel disturbance spectra to satellite pointing stability and evaluates mitigation strategies. A four-wheel pyramid reaction-wheel assembly (RWA) mounted on elastomeric isolators is integrated with a planar air-bearing testbed instrumented with a laser-based optical measurement system. Controlled flywheel unbalance conditions are introduced to excite dominant low-frequency disturbance mechanisms. Measured laser-beam displacement and jitter were analysed in the time and frequency domains and compared with an analytical disturbance model to validate predicted LoS responses. Results confirm that unbalance-related disturbances are the dominant contributor to LoS instability and demonstrate the limited effectiveness of passive isolation at low frequencies, as passive isolators only attenuate excitations above its natural, or cut-off, frequency. The combined modelling, simulation, and air-bearing measurement framework provides a validated method for predicting reaction-wheel-induced micro-vibrations, allocating jitter budgets, and assessing isolation and balancing strategies early in the design cycle of future satellite missions.

Keywords—small satellites, micro-vibrations, reaction wheels, air bearing, jitter, pointing stability, passive isolation

I. INTRODUCTION

Orbital launch cadence has accelerated sharply, driven by declining costs, rapid development cycles, and strong commercial interest in constellations. In 2024, nearly 2900 spacecraft reached orbit, of which 97% were small satellites (≤ 100 kg), up from just 190 in 2015 [1]. Small satellites serve both governmental and commercial operators across Earth observation, communications, meteorology, and technology demonstration missions [2].

Pointing stability requirements vary strongly with mission type. High-resolution Earth observation payloads impose the most stringent demands; Dennehy [2] shows that sub-meter ground sample distances correspond to line-of-sight (LoS)

stability limits of a few milli-arcseconds per second. Platform instability during imaging induces smear, blur, and pixel distortion that complicate downstream processing [3].

Achieving these objectives depends on precise orientation control, provided by an attitude determination and control subsystem (ADCS) that processes sensor measurements and commands actuators [4]. Three-axis control is most commonly achieved using reaction wheels, which are electrically driven flywheels that exchange angular momentum with the spacecraft body to generate propellant-free control torques [5].

Despite their control precision, reaction wheels generate low-frequency micro-vibrations, which manifest as forces and torques emanating from the flywheel during normal operation. These disturbances propagate through the satellite structure and degrade LoS stability for imaging payloads [2]. As imaging systems continue to improve, characterising these disturbances and identifying practical mitigation strategies, through flywheel balancing, structural design, and vibration isolation, has become increasingly important.

Component-level force-torque characterisation is commonly performed using six-axis piezoelectric platforms, such as sensors manufactured by Kistler [3], [4], and [5]. These measurements quantify disturbances generated by the reaction wheel but do not directly translate them into LoS errors. A key gap in current practice is thus transforming the component-level force-torque measurements to spacecraft-level pointing predictions. Air-bearing platforms, which emulate near-frictionless spacecraft rotation about the centre of mass (COM), bridge this gap by enabling direct optical observation of pointing instability during wheel operation.

This paper describes a combined analytical and experimental framework developed as part of a Master of Engineering thesis [6] at Stellenbosch University. The framework encompasses:

- i. an analytical disturbance model for a four-wheel pyramid RWA,

- ii. experimental characterisation using a six-axis Kistler force-torque sensor, and
- iii. a system-level validation using an air-bearing testbed.

This paper describes the air-bearing experimental campaign and its results, with the modelling and Kistler measurements summarised as context for the system-level validation.

II. BACKGROUND

A. Satellite Pointing Stability

Pointing stability is defined as the root mean square (RMS) variation of the line-of-sight (LoS) angular error, expressed in arcseconds (arcsec) over a specified observation period [6]. The impact of reaction wheel-induced micro-vibrations on satellite pointing stability is determined by propagating the generated disturbances through the satellite structure, where factors such as satellite size and mass distribution, structural stiffness, damping properties, and the placement of reaction wheels are critical [2]. In general, LoS pointing errors decrease as satellite size and mass increase, because larger inertias resist angular acceleration more effectively.

Industry requirements for pointing stability have tightened substantially in recent years [6]. In 2017, the JPL 6U CubeSat ASTERIA was deployed with a payload pointing error requirement of 5 arcseconds RMS over 20-minute observation periods, corresponding to approximately 1/30th of a pixel for its imaging payload [7]. The effects of this pointing error on target tracking during coarse and fine pointing control are illustrated in Fig. 1.

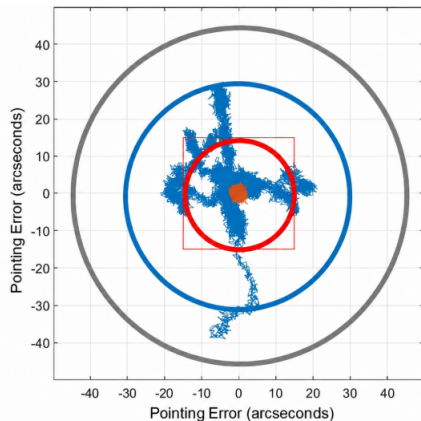


Fig. 1. ASTERIA satellite LoS pointing error during coarse (blue) and fine (red) pointing control over a 20-minute observation period [13].

B. Reaction Wheel Unbalance

Micro-vibrations can be classified as forces and torques that emanate from reaction wheels during standard operation. These forces and torques manifest in the respective degrees of freedom (DoF) of a reaction wheel as F_x , F_y , F_z (N), and T_x , T_y , T_z (Nm).

The disturbance content of small-satellite reaction wheels predominantly occupies the 0Hz–1000Hz frequency band. The dominant disturbance sources in this frequency band are identified as: structural resonance modes, flywheel mass unbalance, motor torque ripple, and ball-bearing imperfections [6]. The first two disturbance mechanisms are incorporated into the disturbance model, as they are inherent to the reaction wheel structure, and occur at frequencies lower than the cut-off frequencies of common passive isolators.

Structural resonance modes refer to the patterns of motion of a system when it is excited at its resonance frequencies. The modes pertain to the reaction wheel structure itself. The fundamental structural resonance modes are defined and shown in Fig. 2. Flywheel unbalance arises when the rotor mass is not symmetrically distributed about the spin axis, and takes two distinct forms: static unbalance and coupled unbalance. In both cases the resulting disturbance peaks once per revolution, so the excited frequencies scale linearly with wheel speed. Fig. 3 illustrates the two unbalance configurations.

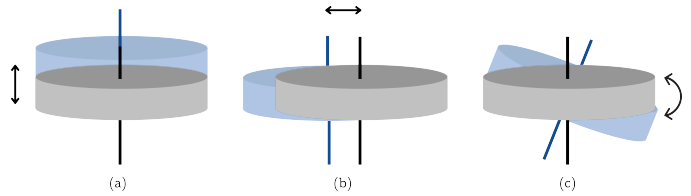


Fig. 2. Visual representation of (a) axial translation mode, (b) radial translation mode, and (c) rocking mode [6].

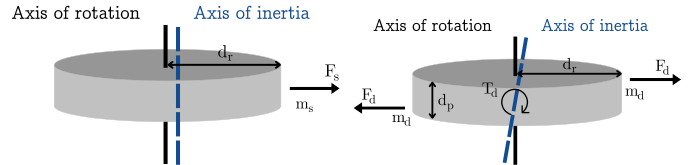


Fig. 3. Visual representation of static (m_s) and coupled (m_d) unbalance mass on a flywheel [6].

Passive elastomer isolators act as mechanical low-pass filters, suppressing high-frequency disturbance energy above their cut-off frequency while passing the low-frequency unbalance content within the attitude control bandwidth [8], [9].

C. Reaction Wheel Disturbance Model

A complete disturbance model for both single and pyramid-configuration reaction wheels is developed in [6], including the effects of unbalance, structural resonance, and passive isolation. The disturbance model follows the methods of Le [10] and Masterson [11], modelling each CubeSpace CW0162 reaction wheel flywheel as a rigid rotating disk supported by two spring-dashpot systems representing the ball bearings.

The final model simulates forces and torques generated by the reaction wheel pyramid assembly placed on passive isolators, as a result of static unbalance, coupled unbalance, and

the three structural resonance modes (axial translation, radial translation, and rocking) across the 0–1000 Hz operational bandwidth.

III. SIMULATING SATELLITE JITTER

Translating RWA-level forces and torques into spacecraft pointing error requires an additional transformation step. This paper derives that link, establishing how reaction-wheel disturbances propagate through the spacecraft’s rotational dynamics to produce measurable LoS jitter.

The transformation is derived under four simplifying assumptions:

- (i) the pyramid RWA aligns with the satellite body coordinate (SBC) frame,
- (ii) roll, pitch, and yaw correspond to rotations about $+X_{SBC}$, $+Y_{SBC}$, and $+Z_{SBC}$,
- (iii) passive isolators limit relevant disturbances to unbalance content below 100 Hz, and
- (iv) the RWA control torque is not considered.

A. Force-to-Torque Transformation

Each reaction wheel in the pyramid configuration generates disturbance forces and torques expressed in its local frame. When these forces act at positions offset from the satellite’s centre of mass (COM), they produce additional moments that contribute to the total disturbance torque on the spacecraft body. The resultant disturbance torque acting on the satellite in the SBC frame, \mathbf{T}_{SBC} (Nm), is expressed as [6]:

$$\mathbf{T}_{SBC} = \sum_{i=1}^4 (\mathbf{T}_{PYR,i} + \mathbf{r}_i \times \mathbf{F}_{PYR,i}) \quad (1)$$

where \mathbf{r}_i (m) is the vector from the satellite COM to the COM of reaction wheel i . The first term captures direct torques, $\mathbf{T}_{PYR,i}$ (Nm), generated by the individual reaction wheel assemblies; the second accounts for moment-arm effects of the transmitted disturbance forces, $\mathbf{F}_{PYR,i}$ (N), generated by the respective reaction wheels [6].

B. Satellite Rotational Dynamics

The disturbance torque \mathbf{T}_{SBC} from (1) excites the rotational degrees of freedom of the spacecraft about its principal inertia axes. Under the assumption that attitude excursions remain within the linear regime, the spacecraft body-frame rotational dynamics are described by the linearised Euler equations:

$$\mathbf{I}_{BODY} \dot{\boldsymbol{\omega}} = \mathbf{T}_{SBC} \quad (2)$$

where \mathbf{I}_{BODY} is the satellite moment-of-inertia tensor and $\dot{\boldsymbol{\omega}}$ is the body-frame angular-rate vector. Double integration of (2) yields the instantaneous angular displacement $\boldsymbol{\theta}(t)$, which represents the small-angle pointing deviation of the spacecraft along its roll, pitch, and yaw axes.

C. Line-of-sight Pointing Error

The angular displacement $\boldsymbol{\theta}(t)$ computed from (2) directly determines the optical LoS deviation of any payload mounted on the spacecraft. The lateral displacement of the projected beam, or image point on the focal plane, is approximated by:

$$\Delta s(t) = L \cdot \boldsymbol{\theta}(t) \quad (3)$$

where L is the projection distance. This translates mechanical disturbances into a directly measurable optical quantity, enabling comparison between simulated predictions and the air-bearing experimental results in Section VI.

IV. EXPERIMENTAL SETUP

A. Hardware and Equipment

The complete list of hardware and equipment used in the air-bearing campaign is listed in TABLE I below, with the physical system layout including annotations shown in Fig. 4.

TABLE I
EXPERIMENTAL HARDWARE AND EQUIPMENT UTILISED.

#	Component	Model	Qty	Function
1	Air bearing	Newway C3650VD02	1	Precision socket providing near-frictionless rotation
2	Semi-sphere ball bearing	Custom design	1	Floats within the socket to enable free rotation
3	Stand	Custom design	1	Structural support for the socket
4	Compressed gas	Nitrogen	1	Supply flow for floating sphere
5	Mounting plate assembly	Custom design	1	Mounting platform with counterweights
6	CubeADCS	—	1	Interface for commanding the reaction wheels and reading telemetry
7	Isolated Pyramid RWA	CW0162	1	Device under test
8	LiPo 14.7 V Battery Pack	Mounted on custom PCB	1	Provides power to the CubeADCS and RWLs
9	Laser Pointer	<5 mW, 635–655 nm	1	Projects displacement measurement beam
10	USB-to-Serial Adaptor PCB	XBee Explorer USB	1	USB-to-Serial converter
11	Radio Antenna	XBee 2 mW PCB Antenna Series 2	2	Wireless serial communication
12	High-speed camera	Fuji X2	1	Capture projected laser displacement
13	Tripod	—	1	Mounting stand for the camera
14	PC with required software	CubeSpace GSE App	1	Communication to CubeADCS

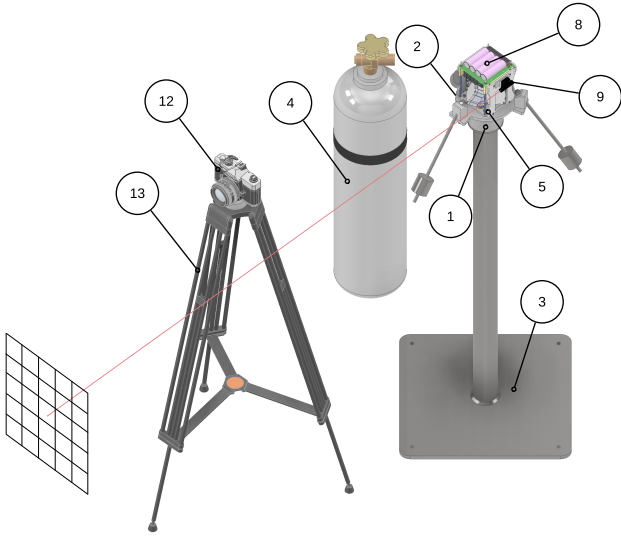


Fig. 4. Experimental air bearing setup with annotations.

B. Test Configuration

The air-bearing campaign test configuration comprises an isolated CubeSpace CW0162 pyramid RWA secured to a custom platform that mates with the air-bearing socket. Initial tests were performed with four balanced wheels previously characterised on the Kistler sensor [6]; under this condition the projected laser showed no measurable displacement over the 2.05 m projection path.

To produce detectable laser displacement over the short projection distance, a controlled unbalance was machined into RWL0 by removing flywheel material. This also extended the lever arm between RWL0's centre of mass and the platform centre of mass with offsets of 38.81 mm (x), 11.42 mm (y), and 20.33 mm (z), in turn magnifying the net disturbance torque. The resulting mounting arrangement, relative to the SBC, is shown in Fig. 5. The physical setup is shown in Fig. 6.

Prior Kistler measurements [6] confirmed that RWL0 dominated the net pyramid disturbance spectrum; the three balanced wheels contributed negligibly.

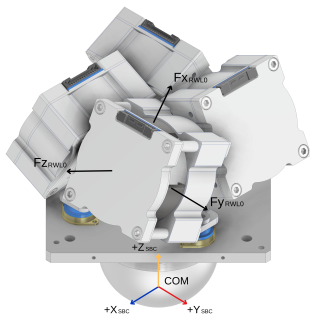


Fig. 5. Isolated pyramid configuration RWA with RWL0 induced unbalance visible.

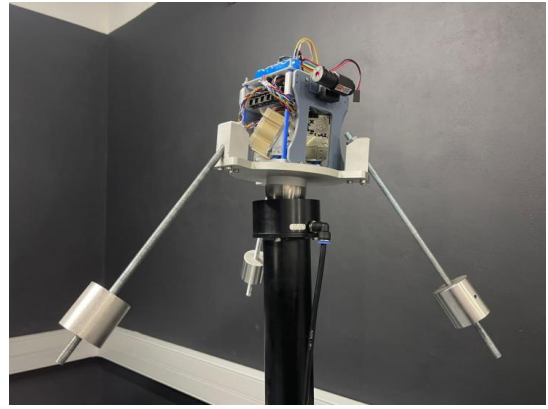


Fig. 6. Isolated pyramid configuration RWA connected to a CubeADCS mounted on an air bearing.

V. MEASUREMENT METHODOLOGY

A. Data Acquisition and Sampling

The testbed couples two parallel data streams: wireless CubeADCS telemetry and optical laser displacement. A wireless UART bridge relays commands and telemetry between the PC and the CubeADCS, leaving the platform free to rotate without cable restraint.

Furthermore, a 240-fps high-speed camera captured the projected laser beam. At this frame rate the Nyquist frequency is 120 Hz, which fully covers the 0–100 Hz unbalance band [12] and eliminates the need for a dedicated high-bandwidth position detector. Post-processing extracted the beam centroid frame by frame, yielding time-domain displacement traces in the yaw and pitch axes that directly quantify platform angular jitter.

The two subsystems together provide synchronised telemetry and optical records, enabling measured LoS errors to be correlated directly with commanded wheel states.

B. Test Protocols

The following tests are conducted using the reaction wheel test configuration shown in Fig. 6:

- i. *Open-loop Momentum Command*: An open-loop momentum command of 0.005 Nms is applied around the platform z -axis, and the resulting steady-state body rate is recorded. The dataset provides an analytical estimate of the system moment of inertia around the z -axis, which is used as an input for the predictive disturbance model described in Section III.
- ii. *Open-loop Speed Command*: An open-loop bias speed command of ± 2000 rpm is commanded to the reaction wheels, and the resulting displacement of the laser beam against the wall captured for time-domain and frequency-domain analysis.

Together the two tests provided both an inertia calibration for the air-bearing platform and a direct observation of RWA-induced pointing disturbances.

VI. RESULTS AND ANALYSIS

A. Z-Axis Moment of Inertia

The moment of inertia of the air bearing assembly about the yaw axis is estimated using the open-loop momentum command test described in Section V.B. The effective z -axis inertia (kg m^2) is calculated analytically, as in [6], using

$$I_z = \frac{h_z}{\omega_z} = \frac{0.005}{8.7\left(\frac{\pi}{180}\right)} = 0.032929 \text{ kg m}^2, \quad (4)$$

where h_z is the commanded momentum about the z -axis (Nms), and ω_z the resulting measured steady-state angular velocity of the assembly around the z -axis (rad/s).

Because the air bearing constrains rotation to the z -axis, only yaw displacement is compared against the disturbance model. The estimated inertia was fed directly into the Section III model so that simulated pointing-error predictions are grounded in the actual platform mass distribution.

B. Laser Beam Displacement

The captured video data is processed frame-by-frame to extract laser centroid coordinates. The laser displacement captured across six consecutive frames is shown in Fig. 7.

Signals were pre-processed with a polynomial baseline removal and a Hampel filter (3σ window), a standard approach for vibration measurements [4]. The corrected yaw and pitch displacement traces over the 10-second acquisition window are shown in Fig. 8 and Fig. 9.

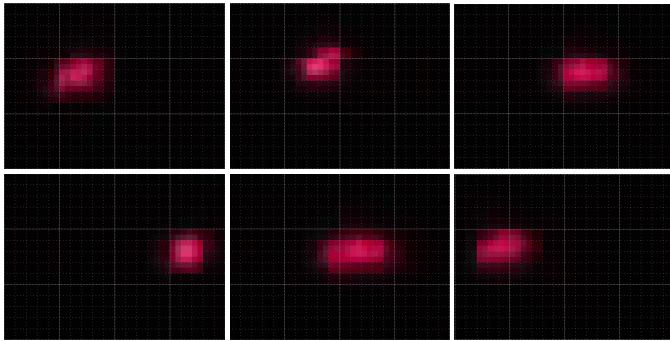


Fig. 7. Projected laser beam displacement over time captured on a high-speed camera.

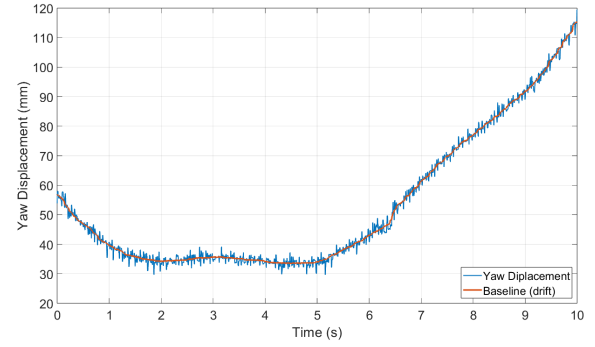


Fig. 8. Measured projected laser beam yaw displacement over time.

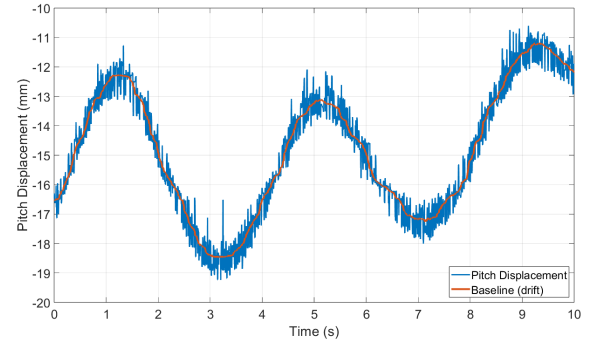


Fig. 9. Measured projected laser beam pitch displacement over time.

C. Laser Beam Jitter

Removing the low-frequency drift component from the corrected signal isolates the high-frequency jitter, which is taken as the measure of platform pointing stability. Fig. 10 shows the jitter scatter over the 10-second window, while Fig. 11 presents the yaw jitter time series.

Fig. 12 shows the FFT of the yaw signal, with a dominant spectral peak at 33.3 Hz, the spin fundamental for 2000 rpm, together with harmonics and subharmonics. The subharmonic content is attributed to mechanical nonlinearities in the modified flywheel and bearing assembly. The flywheel mass was cut away with the flywheel assembled to the motor.

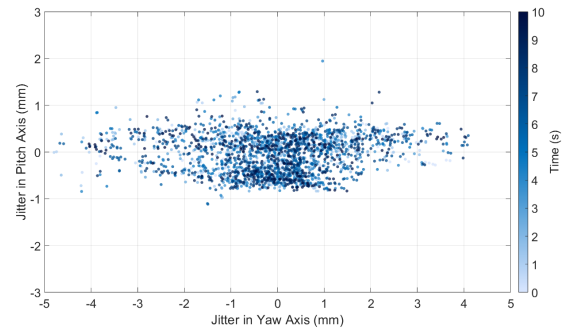


Fig. 10. Scatter plot of measured laser variation in mm, around the baseline drift in yaw and pitch axes over time.

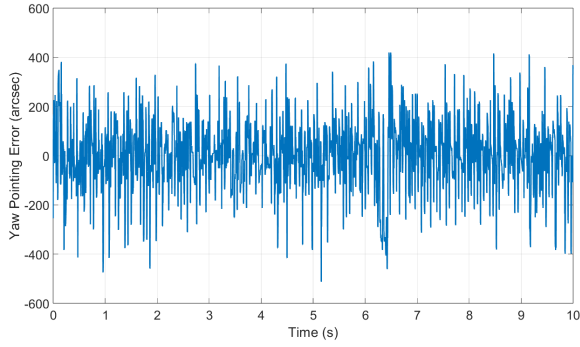


Fig. 11. Measured laser beam variation, or jitter, around baseline drift in the yaw axes over time.

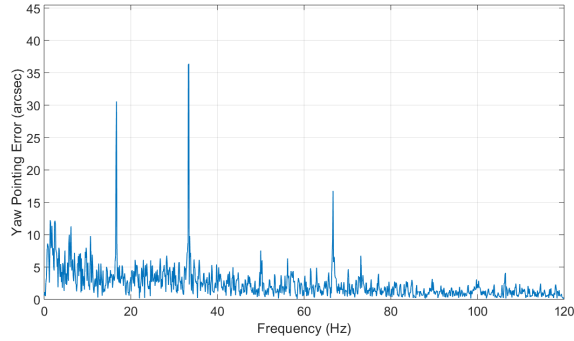


Fig. 12. FFT plot of measured laser beam variation around baseline drift in yaw axes over time.

The disturbance model is then exercised with the parameters in TABLE II to predict platform pointing stability. Unbalance masses are taken from the Kistler characterisation reported in [6]; the z -axis inertia is the analytically estimated value, and the remaining inertia values are set to a representative arbitrary magnitude, as the validation is only performed for the yaw axis.

TABLE II
DISTURBANCE MODEL PARAMETERS REQUIRED FOR POINTING STABILITY PREDICTION.

Parameter	Value	Unit
Equivalent static unbalance mass	[8750 0.2 0.2 0.3]	mg
Equivalent coupled unbalance mass	[950 1.3 0.8 1.5]	mg
Pyramid assembly relative to satellite COM	[0 0 0.052]	m
Satellite moment of inertia matrix	$\begin{bmatrix} 0.037 & 0 & 0 \\ 0 & 0.037 & 0 \\ 0 & 0 & 0.0329 \end{bmatrix}$	kg m^2
Reaction wheel speed	[2000 -2000 2000 -2000]	rpm
Projection distance	2.05	m

Fig. 13 illustrates the simulated displacement due to jitter scatter across the satellite yaw and pitch axes. The displacement in the pitch axis is not considered for comparison, as the moment of inertia of the system in the y -axis is unknown. The scatter's perfect elliptical shape reflects the zero off-diagonal inertia terms assumed in the simulation.

The disturbance model predicts a yaw displacement of 0.45 mm. While the measured amplitude in the time domain was larger, the simulated and experimental FFT spectra agree closely, with yaw jitter predictions within 6 arcsec of one another. The simulated FFT plot is overlaid on top of the measured FFT plot in Fig. 14.

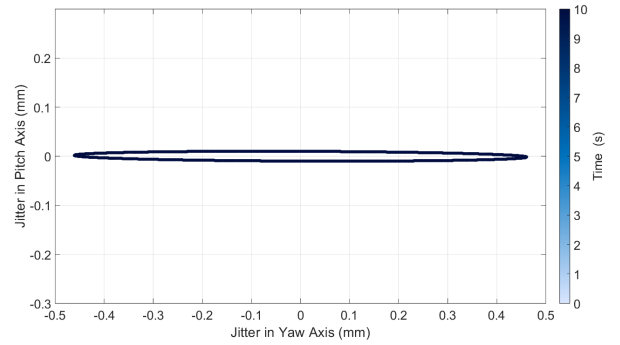


Fig. 13. Scatter plot of simulated laser variation in mm, in yaw and pitch axes over time.

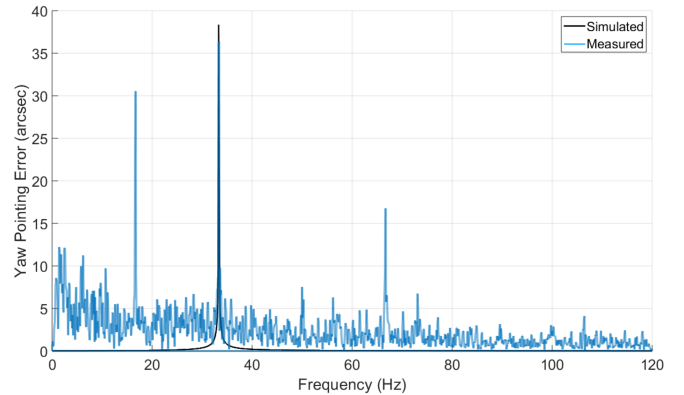


Fig. 14. FFT plot of simulated laser beam variation in yaw axes over time.

The offset in absolute displacement amplitude is attributed to structural resonances excited in the modified flywheel and surface imperfections introduced during manual machining.

VII. CONCLUSION

The air-bearing campaign confirmed that reaction-wheel disturbances translate into measurable LoS pointing errors. With all wheels balanced, jitter across the 2.05 m projection path was negligible. Introducing a large deliberate unbalance into a single wheel of the pyramid assembly produced clearly measurable yaw displacements.

Measured and simulated FFT plots show strong agreement at the spin-frequency fundamental and its harmonics, providing system-level validation of the disturbance model. The results also confirm that passive isolation suppresses resonance-band content but cannot attenuate unbalance-driven disturbances, which couple directly into LoS error. Effective micro-vibration mitigation therefore requires both isolation and flywheel balancing during manufacturing.

The air-bearing measurements close the experimental chain, connecting the subsystem-level Kistler force characterisation [10] to system-level pointing stability predictions that are directly applicable to high-performance imaging mission design.

REFERENCES

- [1] BryceTech, "Smallsats by the Numbers 2025," Mar. 2025. [Online]. Available: <https://brycetek.com/reports/report-documents/smallsats-2025/>
- [2] C. J. Dennehy, "A survey of reaction wheel disturbance modelling approaches for spacecraft line-of-sight jitter performance analysis," in *Proc. European Space Mechanisms and Tribology Symposium*, Munich, Germany, Sep. 2019.
- [3] J. Pan, C. Che, Y. Zhu, and M. Wang, "Satellite jitter estimation and validation using parallax images," *Sensors*, vol. 17, no. 1, p. 83, Jan. 2017.
- [4] W. De Munter, T. Delabie, and D. Vandepitte, "Characterization of reaction wheel micro-vibrations," in *Proc. International Conference on Noise and Vibration Engineering*, Leuven, Jan. 2018, pp. 3511–3525.
- [5] J. Shields, C. Pong, K. Lo, L. Jones, S. Mohan, C. Marom, I. McKinley, W. Wilson, and L. Andrade, "Characterization of CubeSat reaction wheel assemblies," *Journal of Small Satellites*, vol. 6, no. 1, pp. 565–580, May 2017.
- [6] M. du Plessis, "Analysis, simulation, and measurement of micro-vibrations in reaction wheels for high-performance imaging missions," M.Eng. thesis, Dept. Electrical and Electronic Engineering, Stellenbosch University, Mar. 2026.
- [7] C. M. Pong, "On-orbit performance & operation of the attitude & pointing control subsystems on ASTERIA," in *Proc. Small Satellite Conference*, Logan, Utah, Aug. 2018. [Online]. Available: <https://digitalcommons.usu.edu/smallsat/2018/all2018/361/>
- [8] X. Kong, H. Li, X. Zhou, X. Xiang, and X. Shen, "Flywheel vibration isolation of satellite structure by applying structural plates with elastic boundary instead of restrained boundary," *Applied Sciences*, vol. 13, no. 23, Art. no. 12756, Dec. 2023.
- [9] T. Demerville and D. Allaei, "Micro vibration mitigation in space applications," in *Proc. International Conference on Noise and Vibration Engineering*, Leuven, Belgium, Sep. 2020, pp. 3113–3118.
- [10] M. P. Le, "Micro-disturbances in reaction wheels," Ph.D. dissertation, Eindhoven University of Technology, 2017.
- [11] R. A. Masterson, "Development and validation of empirical and analytical reaction wheel disturbance models," Ph.D. dissertation, Massachusetts Institute of Technology, 1999.
- [12] A. V. Oppenheim and R. W. Schaffer, *Discrete-Time Signal Processing*, 3rd ed. London, England: Pearson, 2010.
- [13] H. Alkomy and J. Shan, "modelling and validation of reaction wheel micro-vibrations considering imbalances and bearing disturbances," *J. Sound Vib.*, vol. 492, Feb. 2021, doi: 10.1016/j.jsv.2020.115766.